Article

Predictive Modeling of Corrosion in Al/Mg Dissimilar Joint

Seyedsaied Ahmadvand [1,2,*]**, Mohammadreza Elahifard** [1,*]**, Bijan Peik** [1]**,**
Reza Behjatmanesh-Ardakani [3] **, Behrooz Abbasi** [1] **and Bahman Abbasi** [4,*]

[1]   Department of Metallurgical Engineering, University of Nevada, Reno, Reno, NV 89557, USA
[2]   Department of Chemistry, University of Nevada, Reno, Reno, NV 89557, USA
[3]   Department of Chemistry, Payame Noor University, Tehran 193953697, Iran
[4]   Department of Mechanical Engineering, Oregon State University, Corvallis, OR 97333, USA
[*]   Correspondence: sahamadvad@unr.edu (S.A.); mrelahifard@ardakan.ac.ir (M.E.);
     abbasib@oregonstate.edu (B.A.)

check for
updates

Abstract: In the absence of any abnormality (standard conditions), the gradient of any mechanical/thermodynamic stress would be intensified at the dissimilar joint due to an abrupt change in the chemical composition. This paper aims to investigate the effect of delocalizing this stress by imposing an optimum chemical gradient within the dissimilar joint. In this work, we computationally demonstrated that a homogenous distribution of magnesium atoms in the aluminum (100) structure with a specific chemical gradient could potentially reduce the susceptibility of the Mg/Al dissimilar joint towards micro-galvanic corrosion. This is achieved through the minimization of the work function gradient within the dissimilar joint.

Keywords: work function; Mg/Al dissimilar joint; micro-galvanic corrosion; chemical composition

1. Introduction

Corrosion is a diffusion-controlled process that occurs on the material surface, especially that of metallic dissimilar joints [1–3]. Any mechanical or thermodynamic stress that forms a crack, or any other deficiency, on a system is subject to progressive corrosion, especially at high temperatures [4–6]. The thermal/chemical gradient could trigger this stress [7,8], which is more perceivable in stress corrosion cracking (SCC), where small amounts of reactive chemicals cause disastrous cracking [9]. One can predict the susceptibility of a system to SCC by taking various sources (internal/external) of mechanical and thermodynamic stress into account [9]. Down to the atomic level, the interactions between atoms are different at the interface of two substances A and B, i.e., A–A $\neq$ A–B $\neq$ B–B. Thermodynamically, a drastic drop in the rate of heat flow occurs at the interface of A and B if the difference between their heat capacities (C_p) is significant [10,11]. This causes an isotherm process of phase transition, where the heat is consumed to increase the entropy of the system at the boundary of A and B [12]. The exaggerated version of the first- and pseudo-second-order transition of C_p is shown in Figure 1B for abrupt and progressive chemical transitions. The change in C_p and the density of states (DOS) can be calculated within the phase transition region using the partition functions of the components, which could be an indicator for thermodynamic stress at the boundary of A and B [13,14]. Further, one should consider the geometrical effects to account for the order of degeneracy in the DOS and rate of heat flow. Symmetrical structures have higher degeneracy and thus a higher DOS to disperse the energy, i.e., they can expedite the heat flow and lower the thermodynamic stress [15]. Close-packed structures, e.g., magnesium and aluminum, have lower elasticity and thus less Rayleigh scattering and thermal confusion [16,17]. A and B are potentially able to form more symmetrical and/or

packed structures if they have relatively small and similar atomic radii [18]. Having similar atomic radii, electronegativity, crystal structure, and heat capacity, alloys of aluminum and magnesium (e.g., Al 5000, 6000, and 7000 series) are highly resistant to different types of corrosion [19–21]. In Figure 1A, it is schematically illustrated that if chemical composition changes in a direction perpendicular to the dissimilar joint (y direction), the gradient of the force perpendicular to the plane of the dissimilar joint is maximum with respect to the y direction ($\frac{\partial f_z}{\partial y}_x$). This becomes critical when the perpendicular force is the dominant one, such as in airplane wings and engine blades (Figure 1A) [22–27]. In all aforementioned parameters, the abrupt mechanical and thermodynamic changes at the interface of A and B are the origin of stress in the system. In this sense, similarity in the physicochemical properties of A and B, as well as the minimization of sudden changes in the chemical composition, enhance the durability of the system against corrosion. If two metals are finely manufactured at the dissimilar joint, as in 3D printing, the resulting alloy dissipates the stress of discontinuous force variation as the chemical composition alters from A to B (Figure 1A).
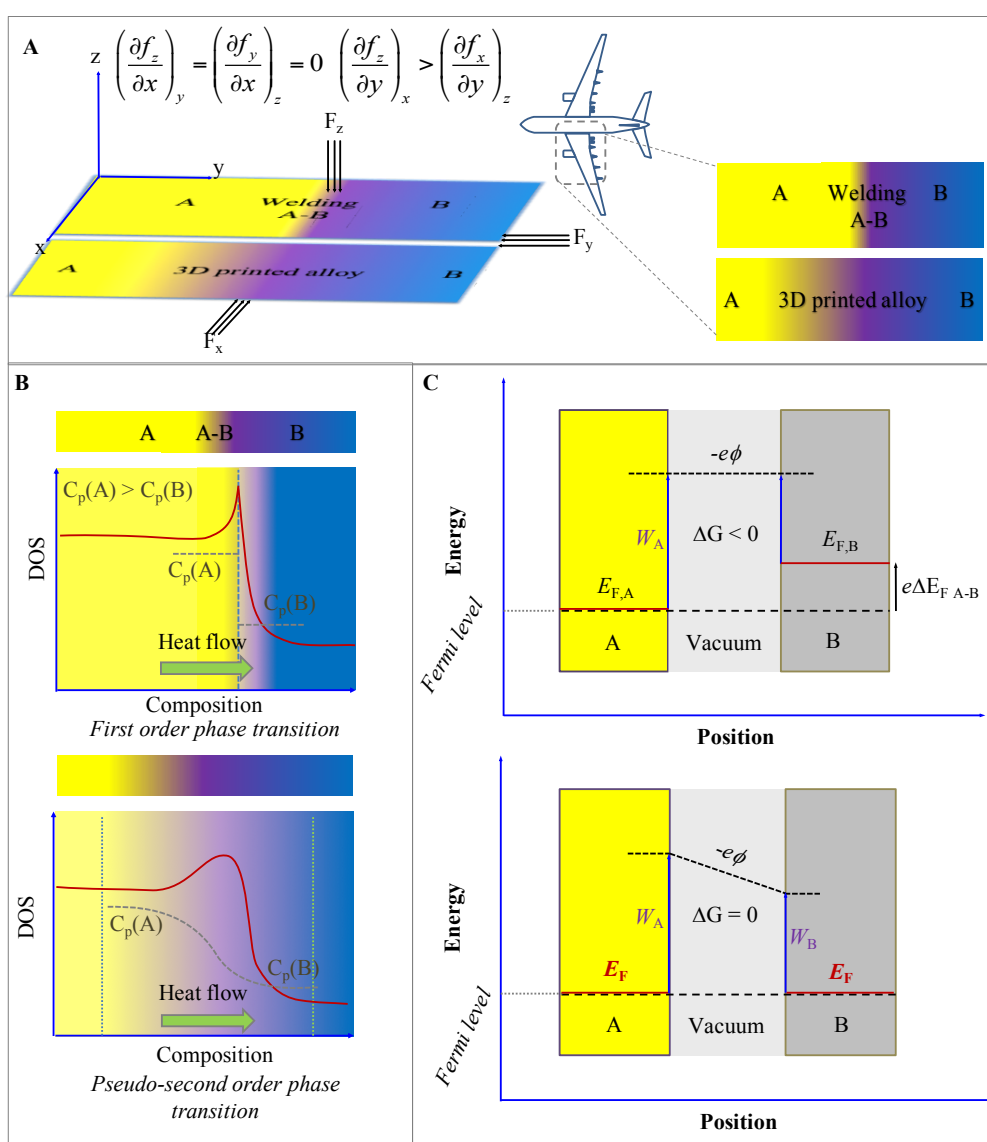

Figure 1. Gradient of force with respect to abrupt (welding) and gradual (3D printing) change of chemical compositions (**A**). Heat flow at a dissimilar joint with two components with different heat capacities (**B**). Electron energy plots against position for two atoms before and at thermodynamic equilibrium (**C**).

A rough estimate for the galvanic corrosion in a dissimilar joint between A and B can be made by taking the difference between the reduction potentials, *E*, or the anodic indices, ΔA_i. In a dissimilar joint, the smaller the electrochemical potential difference between the components, the more compatible the components are to resist galvanic corrosion. For instance, the anodic index of Al (6000 series alloys) is similar to that of low alloy steels ($\Delta A_i = 0.05$ V) and thus the combination of the two is potentially resistant to galvanic corrosion [28]. In a galvanic cell, electrons flow from the anode to the cathode and the cell potential (*E*) is:

$$E_{cell} = E_{Cathode} - E_{anode} \tag{1}$$

As an interfacial parameter, the cell potential is interconnected with the thermodynamic properties by the Nernst equation [29].

$$\Delta G = -nfE \tag{2}$$

In Equation (2), *n* is the number of moles of transferred electrons, *f* is the Faraday constant, and ΔG is the maximum thermodynamic work that can be obtained from the partition functions of the system using quantum computational calculations [30–35].

The electrochemical potential between A and B (Equation (2)) is due to a difference between their Fermi levels before coming into contact (Figure 1C) [36,37]. After A and B are connected and the thermodynamic equilibrium is reached ($\Delta G = 0$), the Fermi levels degenerate and the electrochemical potential vanishes. At this point, corrosion is controlled by the contact potential difference (Volta) that is in turn the difference between the work functions of A and B (Figure 1B) [38]. The micro-galvanic corrosion potential between A and B is the driving force of microscopic corrosion and a trigger for macroscopic corrosion—that is:

$$\Delta E_A^B = \frac{1}{e}\left((\Phi^B - \Phi^A) + (\Phi^B - \Phi^S) + (\Phi^A - \Phi^S)\right) \tag{3}$$

where *e* is the charge of an electron, and Φ^A, Φ^B, and Φ^S are the work functions of A, B, and the standard hydrogen electrode (SHE), respectively [39]. The micro-galvanic corrosion is highly sensitive to the surface state of the system rather than its bulk properties, i.e., any surficial defect or deformation can enhance the corrosion process. The micro-galvanic corrosion can also be measured by a Kelvin probe force microscope (KPFM) [39,40] in order to draw a comparison with the calculated values. The results of the theoretical model are benchmarked with a similar well-known system to obtain the scaling factor. A discrepancy between the theoretical and experimental results (including the scaling factor) can be taken as a criterion of surface roughness.

The fabrication and modeling of the dissimilar joints pose some major challenges: (1) common joining techniques are often inapplicable or more laborious to apply to light metals, such as Al and Mg metals; (2) once joined, the metal pair is very susceptible to different types of corrosion; (3) a detailed knowledge of chemical composition is needed for the precise modeling of corrosion and geometrical effects at the dissimilar joint; and (4) the common approach for modeling the dissimilar joint is the repetition of the unit cell in 3D, which is challenging for varying chemical compositions.

In this paper, density functional theory (DFT) methods were employed to obtain the work functions by calculating the electron density at different regions of the Mg/Al dissimilar joint with different chemical compositions. The results were compared to find the optimum composition of the Mg/Al dissimilar joint that is potentially more resistant to micro-galvanic corrosion. This can be potentially used to fabricate a less corrosive dissimilar joint, assuming that modern fabrication methods, such as 3D printing, are capable of the delicate fabrication of dissimilar joints with defect-free surfaces.

2. Computational Details

DFT methods, using projector-augmented waves (PAWs), have been successfully used in predicting the physical properties of solid materials [41–45]. Herein, a periodic slab model of 2×5 surface unit cells of Al (100) with five layers of 10 atoms, for a total of 50 atoms, was considered, and the vacuum was

set to 30 Å. To make the defective surfaces, Al atoms were substituted by Mg atoms in vertical (parallel to the joint axis) and horizontal layers, as well as homogeneous substitution. All calculations were performed using the Fritz Haber Institute ab initio molecular simulations (FHI-aims) computer program package, which is an all-electron, full potential electronic structure code package [46]. In addition, generalized gradient approximation (GGA), correlation exchange function, and the revised form of the Perdew, Burke, and Ernzerh of method (rPBE) were employed [47,48]. The Monkhorst–Pack grids of $10 \times 10 \times 10$, $3 \times 3 \times 1$, and $20 \times 20 \times 1$ were used for the geometry optimization of the bulk and surface, and the calculation of the work function, respectively. For the surface modeling, two of the layers were frozen while the positions of the remaining atoms were relaxed. On the other hand, nanolayer modeling was performed by the relaxation of all the atoms. In general, the accuracy parameters for the self-consistency cycle were chosen as follows: the convergence criterion for the self-consistency cycle based on the charge density, the sum of eigen values, and the total energy were set to SC_accuracy_rho 10^{-5}, SC_accuracy_eev 10^{-3}, and SC_accuracy_etot 10^{-6}, respectively. The Vienna ab initio simulation package (VASP) was used in all simulations [49].

3. Results and Discussion

Table 1 compares the calculated work functions of pure aluminum and magnesium metals, using the aforementioned optimization methods, with the experimental values. As shown, there is a close agreement between the experimental and calculated values. Table 2 exhibits the simulation results of the work functions for the heterogenous replacement of magnesium atoms parallel to the joint axis (vertical cuts). The results indicate that for the surface optimization, an optimum change in chemical composition is a gradual increment of magnesium atoms from 20 to 40% and thereafter up to 80%. The structure with a lower percentage of magnesium atoms (20%) was more energetically favorable. Twenty percent is the experimental limit for Mg/Al solution. There was no difference between the work functions of top and bottom nanolayers and a slight difference between the work functions of surfaces, which stems from the optimization criteria. This similarity was expected as the chemical composition is the same for top and bottom layers in vertical replacements. According to Table 2, as the percentage of magnesium atom increased, the work function gradually decreased. This trend was followed by all calculated values. However, in horizontal replacements, an oscillation of the work function was obtained as the chemical composition was altered (Table 3). Further, the chemical composition of the top and bottom layers was different, as were the work functions. According to Table 3, this arrangement of atoms and gradient of chemical composition is unlikely to remove the electrochemical stress within the Mg/Al dissimilar joint.

Table 4 represents the homogenous distribution of Mg atoms in the Al (100) structure. According to this table, if the chemical composition of the Mg/Al dissimilar joint changes from 10 to 40% with respect to Mg atoms, the work function would have a smooth transition from its Al value down to its Mg value. This transition had an almost linear trend with 0.2 decrement of the work function per 10% increment of Mg atoms. This minimizes the electrochemical stress and thus the susceptibility to micro-galvanic corrosion. Comparing the energetics of 10 and 20% compositions, the homogenous dissimilar joints were more energetically favorable and thus more stable. For all optimizations, a geometry with 20% of Mg was energetically favorable.

Table 1. Calculated work functions of pure Al and Mg.

Work Function	Mg	Al
Work function (surface)	3.69	3.94
Work function (nanolayer)	3.66	3.94
Work function (experiment)	3.68	4.08

Table 2. Calculated work functions of Mg/Al dissimilar joints with heterogenous and vertical distributions of Mg atoms.
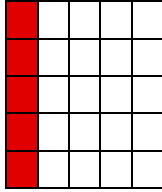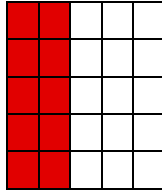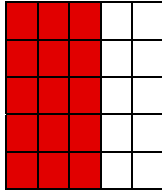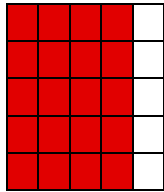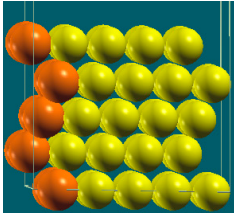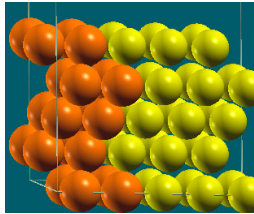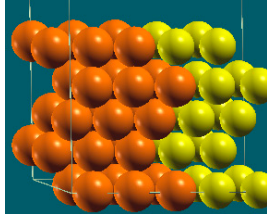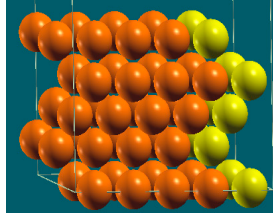
Vertical Cuts				
Structure				
Percentage of Mg atoms (red balls)	20	40	60	80
Work function of the top layer (surface)	3.85	3.70	3.68	3.62
Work function of the bottom layer (surface, eV)	3.84	3.72	3.71	3.65
Energy (eV)	−319,262.69	−307,680.11	−296,098.15	−284,516.63
Work function of the top layer (nanolayer, eV)	3.83	3.69	3.68	3.60
Work function of the bottom layer (nanolayer, eV)	3.83	3.69	3.68	3.60
Energy (eV)	−325,054.31	−319,263.12	−313,472.16	−307,681.56

Table 3. Calculated work functions of Mg/Al dissimilar joints with heterogenous and horizontal distributions of Mg atoms.
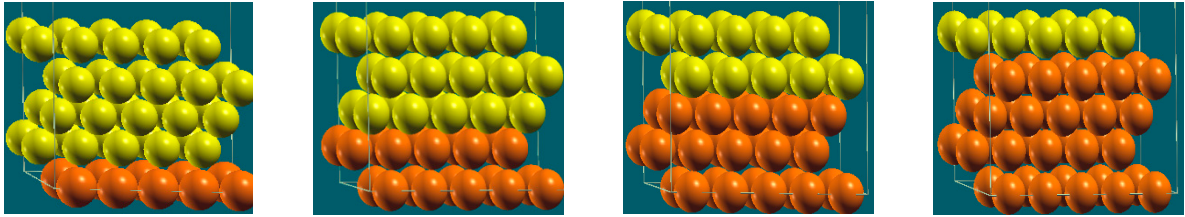
Horizontal Cuts				
Percentage	20	40	60	80
Work function of the top layer (surface)	3.69	3.50	3.65	3.68
Work function of the bottom layer (surface, eV)	3.99	3.97	4.09	4.07
Energy (eV)	−319,262.63	−307,679.54	−296,096.01	−284,513.94
Work function of the top layer (nanolayer, eV)	3.69	3.47	3.57	3.61
Work function of the bottom layer (nanolayer, eV)	3.99	3.95	4.06	4.02
Energy (eV)	−319,262.63	307,679.66	296,097.09	284,514.93

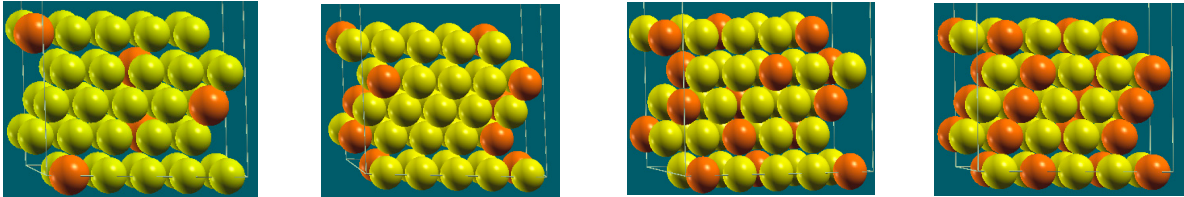**Table 4.** Calculated work functions of Mg/Al dissimilar joints with homogenous distributions of Mg atoms.

Homogenous				
Percentage	10	20	30	40
Work function of the top layer (surface)	3.85	3.75	3.65	3.66
Work function of the bottom layer (surface, eV)	3.85	3.75	3.65	3.67
Energy (eV)	−325,054.22	−319,262.96	−313,471.94	−307,681.31
Work function of the top layer (nanolayer, eV)	3.84	3.75	3.65	3.68
Work function of the bottom layer (nanolayer, eV)	3.85	3.75	3.65	3.68
Energy (eV)	−325,054.31	−319,263.12	−313,472.16	−307,681.56

Figure 2 shows the suggested heterogenous and homogenous chemical compositions of Mg/Al dissimilar joints, according to the work function gradient. The suggested chemical compositions had the lowest work function gradient within the dissimilar joint. This chemical composition changed from 100% down to 40, 20, and 0% Mg in the heterogenous case, and to 20, 10, and 0% in the homogenous case. Overall, the latter case had a smoother work function gradient.
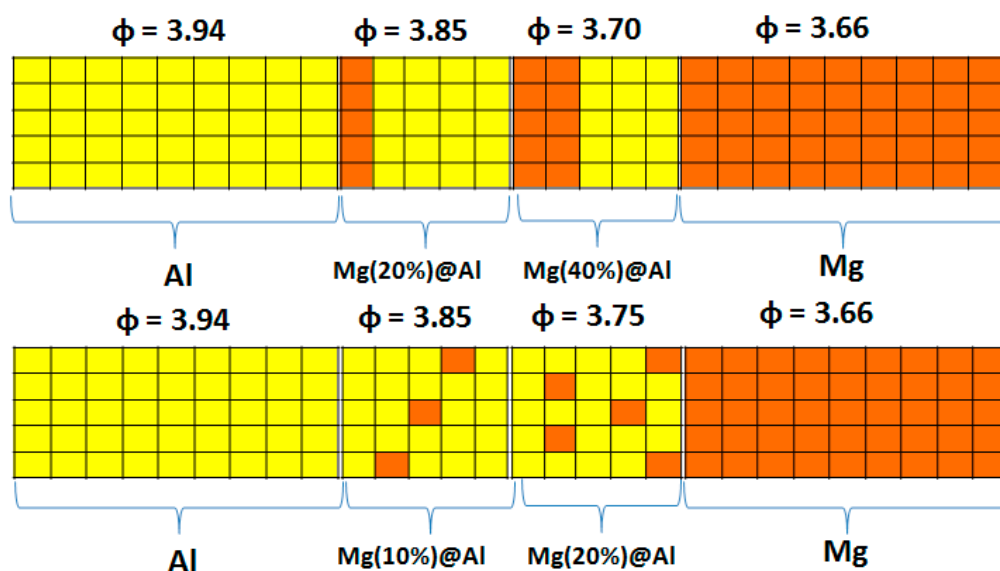

Figure 2. Suggested chemical compositions for the heterogenous (**top**) and homogenous (**bottom**) Mg/Al dissimilar joints.

4. Conclusions

In this research, the effect of chemical gradient in the corrosivity of a Mg/Al dissimilar joint was computationally investigated. This was obtained by comparing the work function gradient within the dissimilar joint as a criterion for micro-galvanic corrosion across three models: (1) the vertical heterogenous distribution of Mg atoms in Al (100), (2) the horizontal heterogenous distribution of Mg atoms in Al (100), and (3) the homogenous distribution of Mg atoms in Al (100). Horizontal distribution resulted in an oscillation of the work function with the change of chemical composition, which was not electrochemically favorable. However, vertical distribution resulted in a rather smoother change in the work function, while the top and bottom layers had the same structures. For the latter model, the work function decreased from its value for pure Al down to that of Mg with the increase of the percentage of Mg atoms. This trend was even smoother for homogenous structures, with an almost linear decrement of work function values. Further, homogenous structures were easier to fabricate and more stable energetically.

Author Contributions: Conceptualization, S.A. and B.A. (Bahman Abbasi); Methodology, S.A. M.E., and R.B.-A.; Software, S.A. M.E., and R.B.-A.; Validation, B.A. (Bahman Abbasi), M.E., and S.A.; Formal Analysis, S.A. and M.E.; Data Curation, S.A. and M.E.; Writing-Original Draft Preparation, S.A.; Writing-Review & Editing, B.A. (Bahman Abbasi), B.P., and S.A.; Visualization, M.E. and S.A.; Supervision, B.A. (Bahman Abbasi) and B.A. (Behrooz Abbasi); Project Administration, B.A. (Bahman Abbasi); Funding Acquisition, B.A. (Behrooz Abbasi) and B.A. (Bahman Abbasi).

Conflicts of Interest: The authors declare no conflict of interest.

References

1. Wang, S.; Ma, Q.; Li, Y. Characterization of microstructure, mechanical properties and corrosion resistance of dissimilar welded joint between 2205 duplex stainless steel and 16MnR. *Mater. Des.* **2011**, *32*, 831–837. [CrossRef]

2. Bosch, R.W.; Bogaerts, W.F. A theoretical study of AC-induced corrosion considering diffusion phenomena. *Corros. Sci.* **1998**, *40*, 323–336. [CrossRef]

3. Melchers, R.E. Mathematical modelling of the diffusion controlled phase in marine immersion corrosion of mild steel. *Corros. Sci.* **2003**, *45*, 923–940. [CrossRef]

4. Gu, B.; Luo, J.; Mao, X. Hydrogen-facilitated anodic dissolution-type stress corrosion cracking of pipeline steels in near-neutral pH solution. *Corros. Eng.* **1999**, *55*, 96–106. [CrossRef]

5. Celis, J.P.; Ponthiaux, P.; Wenger, F. Tribo-corrosion of materials: Interplay between chemical, electrochemical, and mechanical reactivity of surfaces. *Wear* **2006**, *261*, 939–946. [CrossRef]

6. Könönen, M.H.O.; Lavonius, E.T.; Kivilahti, J.K. SEM observations on stress corrosion cracking of commercially pure titanium in a topical fluoride solution. *Dent. Mater.* **1995**, *11*, 269–272. [CrossRef]

7. Ramezanianpour, A.A.; Zolfagharnasab, A.; Zadeh, F.B.; Estahbanati, S.H.; Boushehri, R.; Pourebrahimi, M.R.; Ramezanianpour, A.M. Effect of supplementary cementing materials on concrete resistance against sulfuric acid attack. In *High Tech Concrete: Where Technology and Engineering Meet—Proceedings of the 2017 Fib Symposium*; Springer International Publishing: Basel, Switzerland, 2017; pp. 2290–2298.

8. Boushehri, R.; Hasanpour Estahbanati, S.; Ghasemi-Fare, O. Controlling Frost Heaving in Ballast Railway Tracks Using Low Enthalpy Geothermal Energy. In Proceedings of the Transportation Research Board 98th Annual Meeting, Washington, DC, USA, 13–17 January 2019.

9. Winzer, N.; Atrens, A.; Song, G.; Ghali, E.; Dietzel, W.; Kainer, K.U.; Hort, N.; Blawert, C. A critical review of the Stress Corrosion Cracking (SCC) of magnesium alloys. *Adv. Eng. Mater.* **2005**, *7*, 659–693. [CrossRef]

10. Dubi, Y.; Di Ventra, M. Colloquium: Heat flow and thermoelectricity in atomic and molecular junctions. *Rev. Mod. Phys.* **2011**, *83*, 131–155. [CrossRef]

11. Azad, E.; Peik, B.; Abbasi, B.; Abbasi, B. A numerical simulation of thermo-mechanical behavior of a single fracture in porous rock. In Proceedings of the 52nd U.S. Rock Mechanics/Geomechanics Symposium, Seattle, WA, USA, 17–20 June 2018.

12. Binder, K. Theory of first-order phase transitions. *Rep. Prog. Phys.* **1987**, *50*, 783–859. [CrossRef]

13. Zhang, C.; Ma, J. Simulation via direct computation of partition functions. *Phys. Rev. E Stat. Nonlinear Soft Matter Phys.* **2007**, *76*, 036708. [CrossRef]

14. Irikura, K.K. Anharmonic partition functions for polyatomic thermochemistry. *J. Chem. Thermodyn.* **2014**, *73*, 183–189. [CrossRef]

15. Abed, W.M.; Domingues, A.F.; Poole, R.J.; Dennis, D.J.C. Heat transfer enhancement in a cross-slot micro-geometry. *Int. J. Therm. Sci.* **2017**, *121*, 249–265. [CrossRef]

16. Lutich, A.A.; Gaponenko, S.V.; Gaponenko, N.V.; Molchan, I.S.; Sokol, V.A.; Parkhutik, V. Anisotropic light scattering in nanoporous materials: A photon density of states effect. *Nano Lett.* **2004**, *4*, 1755–1758. [CrossRef]

17. Tata, B.V.R.; Joshi, R.G.; Gupta, D.K.; Brijitta, J.; Raj, B. Crystalline arrays of submicron-sized particles through colloidal route. *Curr. Sci.* **2012**, *103*, 1175–1184.

18. Hellawell, A.; Lu, S.Z. The mechanism of silicon modification in aluminum-silicon alloys: Impurity induced twinning. *Metall. Mater. Trans. A* **1987**, *18*, 1721–1733.

19. Brown, R.; Sprowls, D.; Shumaker, M. The Resistance of Wrought High Strength Aluminum Alloys to Stress Corrosion Cracking. Stress Corrosion Cracking of Metals—A State of the Art. *ASTM Int.* **2009**. [CrossRef]

20. Sanders, R.E. Technology innovation in aluminum products. *JOM* **2001**, *53*, 21–25. [CrossRef]

21. Tsangaraki-Kaplanoglou, I.; Theohari, S.; Dimogerontakis, T.; Wang, Y.M.; Kuo, H.H.; Kia, S. Effect of alloy types on the anodizing process of aluminum. *Surf. Coat. Technol.* **2006**, *200*, 2634–2641. [CrossRef]

22. Liang, J.S.Y.; Su, J.C. Residual stress modeling in orthogonal machining. *CIRP Ann. Manuf. Technol.* **2007**, *56*, 65–68. [CrossRef]

23. Sane, S.P.; Dickinson, M.H. The control of flight force by a flapping wing: Lift and drag production. *J. Exp. Biol.* **2001**, *204*, 2607–2626.

24. Kerschen, G.; Golinval, J.C.; Vakakis, A.F.; Bergman, L.A. The method of proper orthogonal decomposition for dynamical characterization and order reduction of mechanical systems: An overview. *Nonlinear Dyn.* **2005**, *41*, 147–169. [CrossRef]

25. Foolad, F.; Blankenau, P.; Kilic, A.; Allen, R.G.; Huntington, J.L.; Erickson, T.A.; Ozturk, D.; Morton, C.G.; Ortega, S.; Ratcliffe, I.; et al. Comparison of the Automatically Calibrated Google Evapotranspiration Application—EEFlux and the Manually Calibrated METRIC Application. *Preprints* **2018**. [CrossRef]

26. Foolad, F.; Franz, T.E.; Wang, T.; Gibson, J.; Kilic, A.; Allen, R.G.; Suyker, A. Feasibility analysis of using inverse modeling for estimating field-scale evapotranspiration in maize and soybean fields from soil water content monitoring networks. *Hydrol. Earth Syst. Sci.* **2017**, *21*, 1263–1277. [CrossRef]

27. Soleymani, F.; Rezaei, S.M.; Sharifi, S.; Zareinejad, M. Position control of a servo-pneumatic actuator using generalized Maxwell-Slip friction model. In Proceedings of the 4th RSI International Conference on Robotics and Mechatronics(ICORM 2016), Tehran, Iran, 26–28 October 2016; pp. 246–251.

28. Hasson, D.F.; Crowe, C.R. *Materials for Marine Systems and Structures Treatise on Materials Science and Technology*; Academic Press: Cambridge, MA, USA, 2013; p. 28.

29. Kirubakaran, A.; Jain, S.; Nema, R.K. A review on fuel cell technologies and power electronic interface. *Renew. Sustain. Energy Rev.* **2009**, *13*, 2430–2440. [CrossRef]

30. Mohammadrezaei, V.; Ebrahimi, M.; Beyramabadi, S.A. Study of the effect of molecular cluster size alanine concentrations in water by using the activity coefficient method and density functional theory. *Bulg. Chem. Commun.* **2017**, *49*, 147–151.

31. Mohammadrezaei, V.; Ebrahimi, M.; Beyramabadi, S.A. Calculation of concentration of alanine in water using the activity coefficient model and ab initio model. *Bulg. Chem. Commun.* **2017**, *49*, 106–108.

32. Canneaux, S.; Bohr, F.; Henon, E. KiSThelP: A program to predict thermodynamic properties and rate constants from quantum chemistry results. *J. Comput. Chem.* **2014**, *35*, 82–93. [CrossRef]

33. Chakraborty, P.; Ma, T.; Zahiri, A.H.; Cao, L.; Wang, Y. Carbon-Based Materials for Thermoelectrics. *Adv. Condens. Matter Phys.* **2018**, *2018*, 3898479. [CrossRef]

34. Mohammadi Nasab, A.; Wang, D.; Chen, Z.; Shan, W. Buckling shape transition of an embedded thin elastic rod after failure of surrounding elastic medium. *Extrem. Mech. Lett.* **2017**, *15*, 51–56. [CrossRef]

35. Sharifi, S.; Rezaei, S.M.; Tivay, A.; Soleymani, F.; Zareinejad, M. Multi-class fault detection in electro-hydraulic servo systems using support vector machines. In Proceedings of the 4th RSI International Conference on Robotics and Mechatronics(ICROM 2016), Tehran, Iran, 26–28 October 2016; pp. 252–257.

36. Bisquert, J.; Fabregat-Santiago, F.; Mora-Seró, I.; Garcia-Belmonte, G.; Barea, E.M.; Palomares, E. A review of recent results on electrochemical determination of the density of electronic states of nanostructured metal-oxide semiconductors and organic hole conductors. *Inorg. Chim. Acta* **2008**, *361*, 684–698. [CrossRef]

37. Reiss, H. The Fermi level and the redox potential. *J. Phys. Chem.* **1985**, *89*, 3783–3791. [CrossRef]

38. Bergveld, P.; Hendrikse, J.; Olthuis, W. Theory and application of the material work function for chemical on the field principle. *Meas. Sci. Technol.* **1998**, *9*, 1801–1808. [CrossRef]

39. Jin, Y.; Liu, M.; Zhang, C.; Leygraf, C.; Wen, L.; Pan, J. First-Principle Calculation of Volta Potential of Intermetallic Particles in Aluminum Alloys and Practical Implications. *J. Electrochem. Soc.* **2017**, *164*, C465–C473. [CrossRef]

40. Rohwerder, M.; Turcu, F. High-resolution Kelvin probe microscopy in corrosion science: Scanning Kelvin probe force microscopy (SKPFM) versus classical scanning Kelvin probe (SKP). *Electrochim. Acta* **2007**, *53*, 290–299. [CrossRef]

41. Elahifard, M.R.; Behjatmanesh-Ardakani, R.; Ahmadvand, S.; Abbasi, B.; Abbasi, B. A mechanistic study of photo-oxidation of phenol and AB92 by AgBr/TiO$_2$. *Res. Chem. Intermed.* **2019**, 1–12. [CrossRef]

42. Elahifard, M.R.; Ahmadvand, S.; Mirzanejad, A. Effects of Ni-doping on the photo-catalytic activity of TiO$_2$ anatase and rutile: Simulation and experiment. *Mater. Sci. Semicond. Process.* **2018**, *84*, 10–16. [CrossRef]

43. Emami-Meibodi, M.; Elahifard, M.R. Modeling investigation on the thermal conductivity of saturated vapor. *Fluid Phase Equilibria* **2018**, *474*, 14–19. [CrossRef]

44. Farsad, M.; Elahifard, M.R.; Behjatmanesh-Ardakani, R. Full-potential DFT study of CO dissociation on Fe–Cu cluster. *Theor. Chem. Acc.* **2018**, *137*, 142. [CrossRef]

45. Heydari, H.; Elahifard, M.R.; Behjatmanesh-Ardakani, R. Role of oxygen vacancy in the adsorption and dissociation of the water molecule on the surfaces of pure and Ni-doped rutile (110): A periodic full-potential DFT study. *Surf. Sci.* **2019**, *679*, 218–224. [CrossRef]

46. Ren, X.; Tkatchenko, A.; Rinke, P.; Scheffler, M. Beyond the Random-Phase Approximation for the Electron Correlation Energy: The Importance of Single Excitations. *Phys. Rev. Lett.* **2011**, *106*, 153003. [CrossRef]

47. Perdew, J.; Burke, K.; Wang, Y. Generalized gradient approximation for the exchange-correlation hole of a many-electron system. *Phys. Rev. B* **1996**, *54*, 16533–16539. [CrossRef]

48. Perdew, J.; Burke, K.; Ernzerhof, M. Generalized Gradient Approximation Made Simple. *Phys. Rev. Lett.* **1996**, *77*, 3865–3868. [CrossRef]

49. Kresse, G.; Hafner, J. Ab initio molecular-dynamics simulation of the liquid-metalamorphous-semiconductor transition in germanium. *Phys. Rev. B* **1994**, *49*, 14251–14269. [CrossRef]